



# Line filtering for surgical tool localization in 3D ultrasound images



Marián Uherčík<sup>a</sup>, Jan Kybic<sup>a</sup>, Yue Zhao<sup>b,\*</sup>, Christian Cachard<sup>b</sup>, Hervé Liebgott<sup>b</sup>

<sup>a</sup> Center for Machine Perception, Department of Cybernetics, Faculty of Electrical Engineering, Czech Technical University in Prague, Czech Republic

<sup>b</sup> Université de Lyon, CREATIS; CNRS UMR5220; Inserm U1044; INSA-Lyon; Université Lyon 1, France

## ARTICLE INFO

### Article history:

Received 1 April 2013

Accepted 25 September 2013

### Keywords:

3D ultrasound  
Tool localization  
Line filtering  
Biopsy  
RANSAC

## ABSTRACT

We present a method for automatic surgical tool localization in 3D ultrasound images based on line filtering, voxel classification and model fitting. This could possibly provide assistance for biopsy needle or micro-electrode insertion, or a robotic system performing this insertion. The line-filtering method is first used to enhance the contrast of the 3D ultrasound image, then a classifier is chosen to separate the tool voxels, in order to reduce the number of outliers. The last step is Random Sample Consensus (RANSAC) model fitting. Experimental results on several different polyvinyl alcohol (PVA) cryogel data sets demonstrate that the failure rate of the method proposed herein is improved by at least 86% compared to the model-fitting RANSAC algorithm with axis accuracy better than 1 mm, at the expense of only a modest increase in computational effort. The results of this experiment show that this system could be useful for clinical applications.

© 2013 Elsevier Ltd. All rights reserved.

## 1. Introduction

In this paper, we present a method for enhancement and localization of surgical tools such as needles and electrodes in 3D ultrasound (US) images. Thin tool insertion [1] is a part of many surgical procedures such as biopsy [2], brachytherapy [3], breast cancer therapy and diagnostics [4], and neuron activity recording [5]. A localization system can assist the surgeon in the tool insertion procedure by highlighting the tool position, providing navigation assistance with respect to the target, and choosing the proper plane from the 3D volume for visualization; this will become increasingly important as 3D US probes become more widely used. Automatic tool localization is also important for the accuracy and robustness of robotic tool insertion systems.

### 1.1. Existing tool localization techniques

The first devices to localize and guide surgical tools were mechanical instruments [6]. Here, we will focus on techniques based on medical imaging [7], most particularly ultrasound [8], because of its speed, cost effectiveness and non-invasiveness.

Most tool localization techniques for 3D US are based on projections and Hough transform or Radon transform variants [9–15]. One general disadvantage of projection methods is their computational complexity, even though nearly real-time speed can be achieved using multi-resolution [16,17] and Graphics

Processing Unit (GPU) implementation [18]. Mari et al. [19] have proposed a fast approach that first limits the region of a 3D US image, then uses a parallel integral projection (PIP) [14] to locate the position of a small straight tool. A more serious problem is that projection methods are easily confused if other highly echogenic objects are present in the image.

In a previous paper [20], we introduced another type of tool localization technique, which first finds candidate voxels that are likely to belong to the tool and then fits the selected voxels using a parametric model of the tool shape. The model-fitting approach is much faster than projection-based methods because only a small fraction of the voxels is considered. This method is also more general in that it does not assume that the object is straight. Robustness is achieved using RANSAC [21] and a voxel classifier based on voxel intensity and distance from the assumed tool axis; classifier parameters are learned from training data. RANSAC is used to find an approximate solution, which is subsequently refined in a local optimization step. We have shown experimentally [20] that the model-fitting method achieves the lowest failure rate of all the methods tested. Nevertheless, the failure rate obtained is still too high for clinical applications; it can approach 100% on our most challenging data sets (e.g. breast biopsy). In the present work, we show how to decrease the failure rate.

### 1.2. Proposed method

In this paper, we propose to use the shape information provided by line filtering (see Section 2) to improve the automatic localization method presented previously in [20] and described above, particularly

\* Corresponding author. Tel.: +33 4 72 43 82 26.

E-mail address: [yue.zhao@creatis.insa-lyon.fr](mailto:yue.zhao@creatis.insa-lyon.fr) (Y. Zhao).

its robustness with respect to large and bright background structures and noise. More specifically, line filtering was originally used to enhance the structure of the blood vessel. We now use the fact that it can enhance one-dimensional (1D) structures such as a needle or an electrode. This should help remove incorrect (false-positive) detections of other highly echogenic image structures such as locally planar (2D) interfaces with bones or fat tissue, round ball-like (3D) structures or unstructured noise. A secondary benefit of line filtering is the enhancement of visual contrast, which aids localization for human observers.

There are two hypotheses in this study: (a) the intensity of the needle voxels is higher than the surrounding tissue; (b) the shape of the tool is a thin, long, and non-curved cylinder. Bending is typical for thin electrodes (diameter around 0.3 mm). Biopsy needles are thicker (diameter around 1 mm) and therefore remain straight.

We review existing line-filtering methods in Section 2 and describe our new tool localization algorithm in Section 3. Section 4 contains experimental evaluation and Section 5 shows the results of the complete localization method. Finally, Sections 6 and 7 give the discussion and conclusion, respectively.

## 2. Line-filtering methods

Line filtering is a method for enhancement of 1D line structures, originally developed for vessel enhancement and detection [22]. Here, the tool diameter is fixed and known, which makes the task slightly easier.

A matching filter approach applies a set of similarly shaped filters as the object being sought. Chaudhuri et al. [23] used matched filters for detection of blood vessels in 2D images. In their method, 12 orientations with an angular distance of  $15^\circ$  are considered, and the kernel width  $\sigma$  is determined manually. The method reported by Hoover et al. [24] is based on Chaudhuri's method, and they improved it by using the optimized value of  $\sigma$ . The threshold probing procedure proposed by Hoover et al. classifies each pixel using local- and region-based properties. The response of the matched filter is examined by iteratively decreasing the threshold of the classifier. The accuracy for methods based on a matched filter depends on the number of filters, but the more filters there are, the lower the calculation speed is. The size of the convolution mask also influences the localization speed.

Compared to matched filters, steerable filters [25] are a computationally efficient approach for evaluating responses for many angles by interpolating between responses of only a small number of basic filters. Freeman et al. [25] introduced the design of the steerable filter and provided several application examples. Gonzalez et al. [26] used the steerable filter for line detection in 3D MRA images. They first used the steerable features for statistical 3D dendrite detection. Finally, a

classifier was learned to adapt the filter to particular properties of filaments without manual intervention.

Linear structures can also be seen as ridges in the corresponding higher dimensional space. Aylward et al. [27] approximated the medial axes of tubular vessels as oriented intensity ridges. Ridges are tracked from a user-supplied starting point by estimating the local directions of the tube with respect to the Hessian matrix. The local widths of the object are estimated using points on the ridges. Staal et al. [28] used a Hessian-based method to detect ridges in 2D images followed by a learnable selection scheme. Ridge pixels are grouped by the similarity of eigenvector directions, and straight line elements are formed out of them. The image is partitioned according to the closest line element. Uherčík et al. [29] showed that the elements of the Hessian matrix also constitute a basis for a steerable filter. In next section, the Hessian-based analysis is described.

### 2.1. Hessian-based analysis

Local intensity variations are analyzed via second-order derivatives assembled in a Hessian matrix:

$$M(\mathbf{x}) = \begin{bmatrix} I_{xx}(\mathbf{x}) & I_{xy}(\mathbf{x}) & I_{xz}(\mathbf{x}) \\ I_{yx}(\mathbf{x}) & I_{yy}(\mathbf{x}) & I_{yz}(\mathbf{x}) \\ I_{zx}(\mathbf{x}) & I_{zy}(\mathbf{x}) & I_{zz}(\mathbf{x}) \end{bmatrix} \quad (1)$$

where the partial derivatives  $I_{\cdot\cdot}(\mathbf{x})$  of the volume  $I$  are computed after smoothing with an isotropic Gaussian at scale  $s$  [22], which corresponds to the expected diameter of the linear structure to be detected. Let  $|\lambda_1| \leq |\lambda_2| \leq |\lambda_3|$  be the eigenvalues of the Hessian  $M$ . For a line-like object, the smallest eigenvalue  $\lambda_1$  is small and the corresponding eigenvector  $\mathbf{e}_1$  points along the object's axis. The other two eigenvalues are larger and of approximately the same magnitude for axially symmetric objects, leading to the following condition for the object voxels:

$$(0 \approx |\lambda_1|) \text{ and } (|\lambda_1| \ll |\lambda_2|) \text{ and } (\lambda_2 \approx \lambda_3) \quad (2)$$

There are various ways to combine the eigenvalues into a single scalar measure [30,31]. We choose a measure proposed by Frangi et al. [22]:

$$J(\mathbf{x}) = (1 - e^{-\mathcal{R}_A^2/2\alpha^2})(e^{-\mathcal{R}_B^2/2\beta^2})(1 - e^{-S^2/2\gamma^2}) \quad (3)$$

$$\text{with } \mathcal{R}_B = \frac{|\lambda_1|}{\sqrt{|\lambda_2\lambda_3|}}, \quad \mathcal{R}_A = \frac{|\lambda_2|}{|\lambda_3|}, \quad (4)$$

$$S = \|\mathcal{H}\|_F = \sqrt{\sum_{j=1,2,3} \lambda_j^2} \quad (5)$$

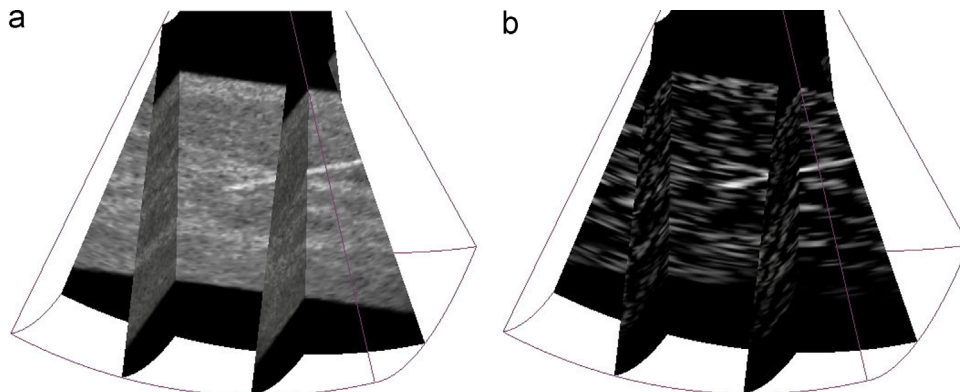
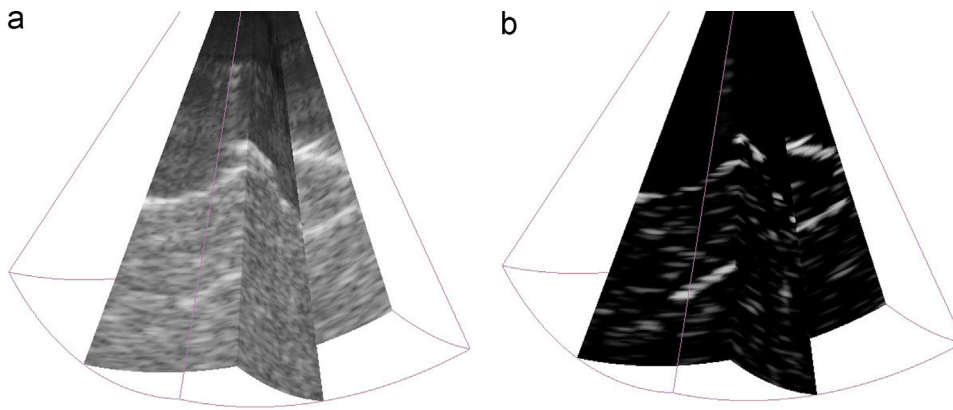


Fig. 1. Example of the line filtering results with a straight needle: (a) original 3D US image simulated using FIELD II and (b) the output of line filtering using Frangi's method.



**Fig. 2.** Example of the line-filtering results: (a) original 3D US image of the PVA cryogel phantom acquired with the Voluson 530D scanner and (b) the output of line filtering using Frangi's method.

Here,  $\mathcal{R}_B$  is used to distinguish the structure from a blob-like pattern;  $\mathcal{R}_A$  distinguishes between the plane-like and line-like structures;  $\mathcal{S}$  quantifies the amount of local structure. As recommended by Frangi et al., the parameters  $\alpha$  and  $\beta$  are set to 0.5; the parameter  $\gamma$  is tuned on training data as described in [22]. As for a bright object on a dark background,  $\lambda_2$  and  $\lambda_3$  should be negative, so  $J$  is set to 0 when  $\lambda_2 \geq 0$  or  $\lambda_3 \geq 0$ . Examples in Figs. 1–3 visually demonstrate the performance of the Frangi measure.

## 2.2. Oriented filters

Oriented filters are designed to give a high response for a linear structure with a particular orientation. The orientation is either known or is assumed to be equal to the normalized eigenvector  $\mathbf{e}_1$  of the Hessian matrix. A standard line filter is [25]

$$\zeta(\mathbf{x}) = \frac{\partial^2 I}{\partial \mathbf{e}_2^2}(\mathbf{x}) + \frac{\partial^2 I}{\partial \mathbf{e}_3^2}(\mathbf{x}), \quad (6)$$

where  $\mathbf{e}_2, \mathbf{e}_3$  are the two eigenvectors perpendicular to  $\mathbf{e}_1$ . In the present application, Eq. (6) is used to calculate the orientation parameter  $\zeta(\mathbf{x})$  and is further used as an extended feature vector.

Note that second-order directional derivatives are easily obtained from the Hessian matrix at a low computational cost:

$$\frac{\partial^2 I}{\partial \mathbf{v}^2}(\mathbf{x}) = \mathbf{v}^T \mathcal{H}(\mathbf{x}) \mathbf{v}, \quad \mathbf{v} \in \mathbb{R}^3, \quad \|\mathbf{v}\| = 1 \quad (7)$$

## 3. Tool localization with line filtering

The main improvement over our previous work [20] is that the first two steps now use the shape information and classifiers trained on labeled training data, which significantly improves localization robustness. It consists of the following four steps:

1. Voxel classification – a set of possible tool voxels  $\mathcal{X}_t$  is chosen using the intensity of the voxels, and the Frangi measure  $J(\mathbf{x})$  (Section 3.1).
2. Axis estimation – an approximate position of the tool axis, defined by a polynomial curve with parameters  $\mathbf{H}$  is found using RANSAC [21], maximizing the number of inliers.<sup>1</sup> Whether or not a voxel is an inlier is classified using the extended features, for example, oriented filter output  $\zeta(\mathbf{x})$  (Section 3.2).

<sup>1</sup> Inliers are points consistent with the model for any set of parameters [32].

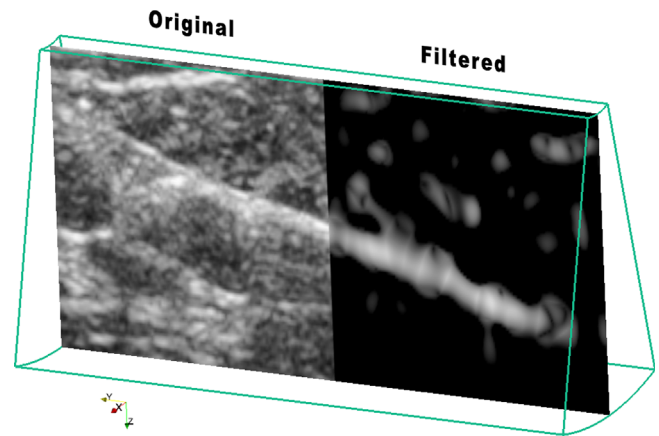


**Fig. 3.** 3D volume of breast biopsy with needle. The left part of the slice contains the original data and the right part contains the data filtered using Frangi's method [22]. The original data were acquired with a GE Voluson E8 scanner.

3. Local optimization – the final solution  $\mathbf{H}^*$  is found by minimizing the mean squared distance of the inliers identified in the previous step from the tool's axis (Section 3.3).
4. Tip localization – the endpoint of the tool is determined by robustly searching for a significant drop in voxel intensity along the axis [14].

### 3.1. Voxel classification

Possible tool voxels  $\mathcal{X}_t$  are selected based on a two-dimensional feature vector  $\mathbf{m}_1(\mathbf{x}) = [I(\mathbf{x}) J(\mathbf{x})]$ , with voxel intensity  $I(\mathbf{x})$  and line-filtering output  $J(\mathbf{x})$ . The following classifiers were tested (see Section 4.2 for experimental comparison):

- (a) A *monolithic linear classifier* [33] trained by Fisher's linear discriminant (FLD), using the feature vector  $\mathbf{m}_1(\mathbf{x})$ ; a pocket training algorithm [34] is also implemented to keep the best solution found so far.
- (b) *Support Vector Machine (SVM)* uses the kernel function with linear mapping [33], which is composed of the  $\mathbf{m}_1(\mathbf{x})$  and a randomly chosen subset from the trained data. The SVM classifier is trained using a fast-cutting plane algorithm [35].
- (c) The *AdaBoost* (adaptive boosting) classifier is actually a learning meta-algorithm [36]. Given a labeled training set and a set of weak classifiers, the AdaBoost produces a strong classifier.

In our method, it is trained with decision stumps [37] and ten weak classifiers.

- (d) **Waldboost** [38] is an algorithm that integrates the AdaBoost training with Wald's sequential probability ratio test (SPRT). Waldboost is trained with domain partitioning weak classifiers [39] with eight bins. The desired TP rate and FN rate (Table 2) were set to 99% and 1%, respectively.
- (e) **The cascaded classifier** consists of two steps. First, the voxels are thresholded, based solely on intensity  $I(\mathbf{x})$ ; the threshold is chosen such that on training data 80% of true positives are retained. The second step is a linear classifier using both  $I(\mathbf{x})$  and  $J(\mathbf{x})$ . The advantage is that the computationally expensive line filtering can only be performed on a small fraction of the pixels, so the classifier is very fast.

### 3.2. Axis estimation

The tool axis is represented by a polynomial parametric curve:

$$a(t; \mathbf{H}) = \underbrace{\begin{pmatrix} h_{11} & \dots & h_{1n} \\ h_{21} & \dots & h_{2n} \\ h_{31} & \dots & h_{3n} \end{pmatrix}}_{\mathbf{H}} \begin{pmatrix} 1 \\ t \\ \vdots \\ t^{n-1} \end{pmatrix}; \quad t \in \mathbb{R} \quad (8)$$

with  $3n$  parameters  $\mathbf{H}$  [20]. We typically use  $n=2$  for straight needles.

Robust estimation of the parameters  $\mathbf{H}$  is based on RANSAC [21]: in each iteration,  $n$  points are randomly chosen and the model is fitted [20] by solving the system of  $3n$  linear equations (8). The number of inliers consistent with the estimated model is counted and at the end, the model consistent with the largest number of inliers is reported. The number of iterations is determined automatically, given the probability the system allows of missing the optimum [20]. Whether or not a point (voxel)  $\mathbf{x}$  is an inlier is determined by another classifier, using an extended feature vector:

$$\omega = [I(\mathbf{x}) \ J(\mathbf{x}) \ d(\mathbf{x}; \mathbf{H}) \ \zeta(\mathbf{x}; \mathbf{H})] \quad (9)$$

containing the voxel intensity  $I$ , tubularity  $J$ , approximate Euclidean distance  $d(\mathbf{x}; \mathbf{H})$  of  $\mathbf{x}$  to the axis described by  $\mathbf{H}$  [20], and the oriented filter output  $\zeta$  (6). Note that both  $d$  and  $\zeta$  are dependent on the current model: for  $\zeta$  we use the local axis orientation in the point closest to  $\mathbf{x}$ . Classifiers (a)–(d) from the previous section were considered, trained on images with manually determined ground truth.

**Table 1**

Mean CR improvement (12) for the three line-enhancement methods and three groups of experiments. The best result in each row is set in bold. Numbers in parentheses give the number of volumes in each data set.

Data type (number)	Frangi	Sato	Li
Simul. (28)	<b>3.14</b>	1.96	0.65
PVA (8)	<b>16.78</b>	4.04	3.12
Breast (3)	<b>4.54</b>	2.29	1.89

**Table 2**

Confusion matrix illustrates naming conventions for the evaluation of classification results.

	Negative predicted	Positive predicted
Actual negative	True negative (TN)	False positive (FP)
Actual positive	False negative (FN)	True positive (TP)

### 3.3. Local optimization

The final solution  $\mathbf{H}^*$  is found by minimizing the mean squared distance of the inliers identified in the previous step from the tool axis:

$$\mathbf{H}^* = \underset{\mathbf{H}}{\operatorname{argmin}} \sum_{\mathbf{x} \in \mathcal{X}_{\text{inl}}} d(\mathbf{x}; \mathbf{H})^2 \quad (10)$$

The optimization is carried out using a derivative-free Nelder–Mead downhill simplex method [40].

## 4. Evaluation of the method

### 4.1. Visual enhancement

The Frangi's method provided visually better results than the other tested methods. To evaluate the improvement objectively, we used the contrast ratio (CR)  $\Psi(I, \mathcal{X}_t, \mathcal{X}_{\text{bg}})$ , defined as the ratio of the mean intensity of the tool voxels  $I(\mathcal{X}_t)$  and the mean intensity of the background (non-tool) voxels  $I(\mathcal{X}_{\text{bg}})$ :

$$\Psi(I, \mathcal{X}_t, \mathcal{X}_{\text{bg}}) = \frac{\operatorname{mean}(I(\mathcal{X}_t))}{\operatorname{mean}(I(\mathcal{X}_{\text{bg}}))} \quad (11)$$

The improvement in CR between the original image of intensity  $I_o$  and the filtered image of intensity  $I_f$  is given by

$$\Psi^{\text{Impr}} = \frac{\Psi(I_f, \mathcal{X}_t, \mathcal{X}_{\text{bg}})}{\Psi(I_o, \mathcal{X}_t, \mathcal{X}_{\text{bg}})} \quad (12)$$

The best improvement in CR is obtained with Frangi's method (Table 1). The computation time is dominated by filtering and calculating the eigenvalues, depends linearly on the number of voxels, and is almost identical for all methods (about 10 s for the simulated data using our Matlab implementation [29]).

**Table 3**

Classifier performance in distinguishing tool voxels. Specificity was set at 80%.

Type of classifier	Mean precision (%)	Mean sensitivity (%)	Specificity (%)
Thresholding	6.0 ± 2.0	32.7 ± 9.1	80
Linear (FLD.)	87.5 ± 1.7	78.8 ± 3.0	80
SVM	88.5 ± 1.7	82.1 ± 3.2	80
AdaBoost	89.0 ± 2.5	90.0 ± 3.9	80
WaldBoost	88.5 ± 1.3	83.2 ± 2.6	80
Cascade	97.8 ± 0.9	46.9 ± 8.1	80

**Table 4**

Time spent on line filtering for different data sets for the line filtering evaluated everywhere (full) and only for voxels selected by the first step of the cascade classifier (cascade).

Data sets	Size (voxels)	Full (s)	Cascade (s)
Simul.	53 × 71 × 164	10.6	<b>1.0</b>
PVA	53 × 71 × 310	18.8	<b>2.1</b>
Breast tissue	383 × 273 × 208	236.7	<b>14.0</b>

**Table 5**

The performance of the inlier classifier on simulated data.

Type of classifier	Precision (%)	Sensitivity (%)	Specificity (%)
Linear (FLD)	94.5 ± 4.4	86.4 ± 4.7	98
SVM	99.1 ± 1.9	99.7 ± 1.1	98
AdaBoost	84.5 ± 5.6	42.8 ± 4.7	98
WaldBoost	97.4 ± 3.1	91.6 ± 8.9	98



#### 4.2. Segmentation evaluation

We compared the ability of classifiers from Section 3.1 to distinguish between tool and background voxels on the simulated data.

The classifiers' working points were adjusted so that their specificity was 80% on the test data:

$$\text{Specificity} = \frac{\text{TN}}{\text{TN} + \text{FP}} \quad (13)$$

where the symbols are defined in Table 2. The main performance criterion is precision (also called inlier ratio or positive predictive value, a voxel is considered to be an inlier if it is closer to the tool axis than the tool radius) because it directly influences RANSAC performance. It is defined as

$$\text{Precision} = \frac{\text{TP}}{\text{TP} + \text{FP}} \quad (14)$$

We also evaluate the sensitivity (TP rate):

$$\text{Sensitivity} = \frac{\text{TP}}{\text{FN} + \text{TP}} \quad (15)$$

For the cross validation, 18 simulated data sets were generated using FIELD II [41,42], with the needle orientation from 40° to 110° with respect to the probe, with 4° steps. Fifty simulation runs are done on the different pairs of training and testing data sets. For each pair of data sets, 12 out of the 18 are used for training, and the remaining six for testing.

**Table 6**  
Parameters used in FIELD II simulations.

Parameter name	Value
Transducer center frequency (MHz)	7.5
Sampling frequency (MHz)	27
Speed of sound (m/s)	1540
Elements of the probe	128
Width of element (mm)	0.1
Height of element (mm)	10
Kerf (mm)	0.017
Focal depth (mm)	50
Range of scan lines (degree)	[−20 20]
Range of scan planes (degree)	[−20 20]

**Table 7**  
Mean contrast ratio improvement (12) for the three line-enhancement methods using the simulated volume with a curved needle. Frangi's method has the best performance.

Data type (number)	Frangi	Sato	Li
Simul. curved (4)	<b>4.25</b>	2.97	2.71

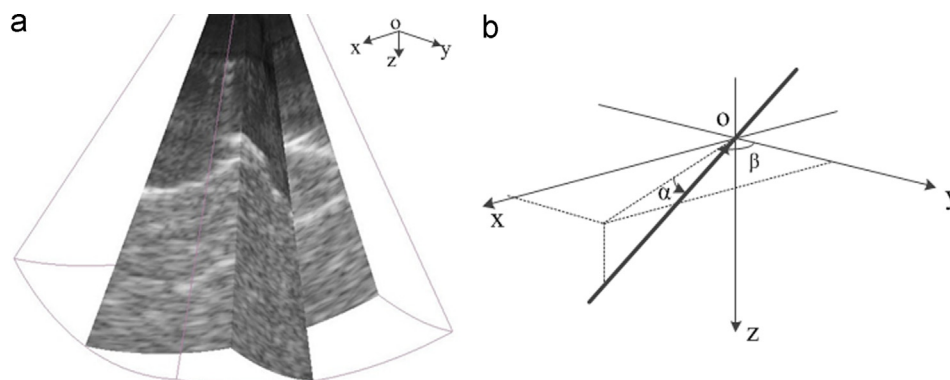


**Fig. 4.** The definition of the needle's two direction angles.

For each run, the training and testing data sets are randomly chosen from the 18 data sets, with no repetition. Table 3 shows the segmentation performance of the different classifiers. The mean precision and sensitivity and their standard deviations are given for 80% specificity. From Table 3, we see that the AdaBoost classifier gives the best results in terms of sensitivity. The cascade classifier has much lower sensitivity but excellent precision, which is important for the subsequent RANSAC step, and the speed gain is substantial (Table 4). The differences between the sensitivity of the linear, SVM, AdaBoost and WaldBoost classifiers was not found to be significant on the *t*-test. All classifiers using line filtering perform significantly better than the previous method [20] that uses only intensity (denoted 'Thresholding' in Table 3).

#### 4.3. Inlier detection

The inlier detector for RANSAC (Section 3.2) was trained and tested using cross-validation (Section 4.2) on synthetic data taking advantage of the availability of ground truth. The position of the tool was chosen randomly with the angle of the tool with respect to the probe axis 40°–110° and the distance of the tool from the probe 30–60 mm. The results for 98% specificity are reported in Table 5. The best performers were the SVM and WaldBoost.

### 5. Results on the tool localization method with line filtering

#### 5.1. Data set used to evaluate the method

The proposed localization method based on line filtering and other state-of-the art methods were implemented in MATLAB (the

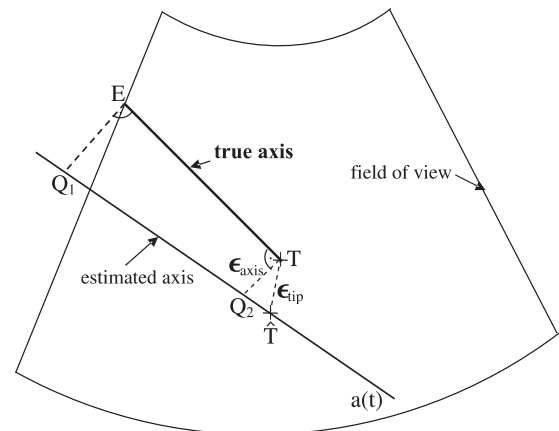


**Fig. 5.** Illustration of the axis accuracy evaluation. The axis accuracy  $\epsilon_{\text{axis}}$  is defined as the maximum Euclidean distance between the true endpoints and their projections on the estimated tool axis. The tip accuracy  $\epsilon_{\text{tip}}$  is the Euclidean distance between the true tip and the estimated tip.

MathWorks, Natick, MA, USA) and tested on a PC with an Intel Core 4 processor at 2.83 GHz. The results of the experiments compare the various methods on the following data sets.

**Simulation:** Twenty-eight 3D US data sets were generated by an ultrasound simulator FIELD II [41,42] with the tool's ground-truth location known (Fig. 1a). Table 6 gives the parameters used in FIELD II, set to mimic the real ultrasound scanner as closely as possible.

An image of a needle was created by adding a 0.6-mm-diameter cylinder with highly reflecting scatterers. For each 3D image, there were 53 azimuthal planes covering an angle of  $40^\circ$

and 71 planes covering a lateral angle of  $40^\circ$ ; in the axial direction, each pixel corresponds to approximately 0.1 mm.

**PVA phantom:** Experiments were conducted on a PVA cryogel phantom [43] that mimics biological tissue properties.

The PVA cryogel phantom contained a 0.3-mm-diameter electrode. It is important to note that although the real diameter of the electrode is 0.3 mm, the apparent diameter in the US volume will be almost the same as the simulated one because ultrasound images convolve with the point spread function (PSF) [19] (Fig. 2a). Eight 3D US images,  $53 \times 71 \times 260$  voxels, of the PVA cryogel phantom with different

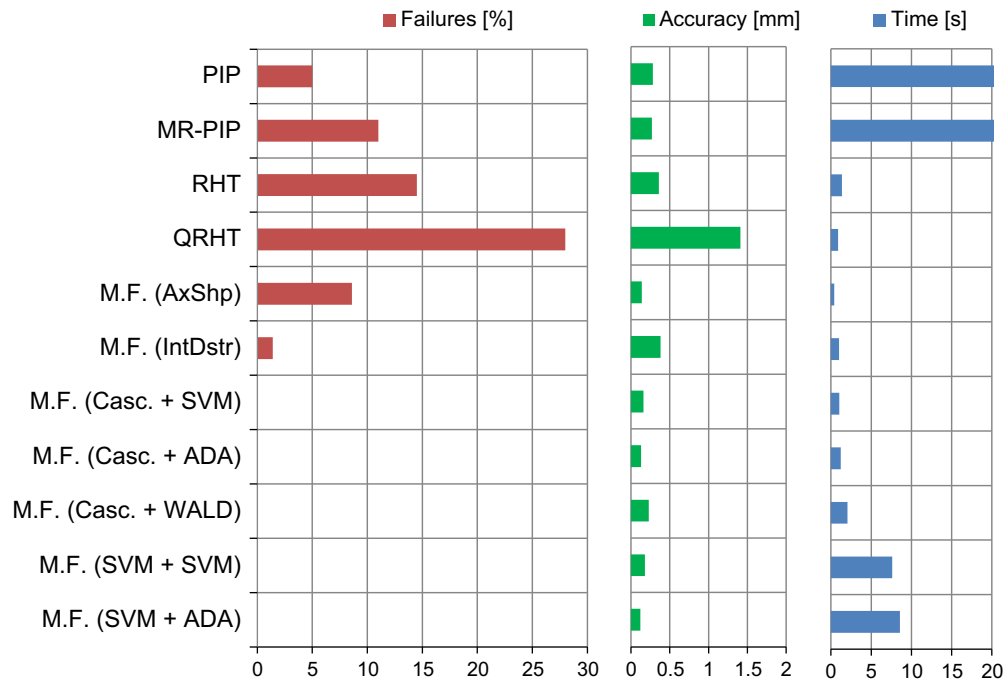


**Fig. 6.** The results of the tool localization on simulated data with high contrast ratio (CR) ( $CR=1.7$ ). M.F. stands for model-fitting (RANSAC) methods. The first column is the failure rate for all the methods expressed as a percentage; the second column is the axis accuracy in mm; the third column is the calculation time for each method.

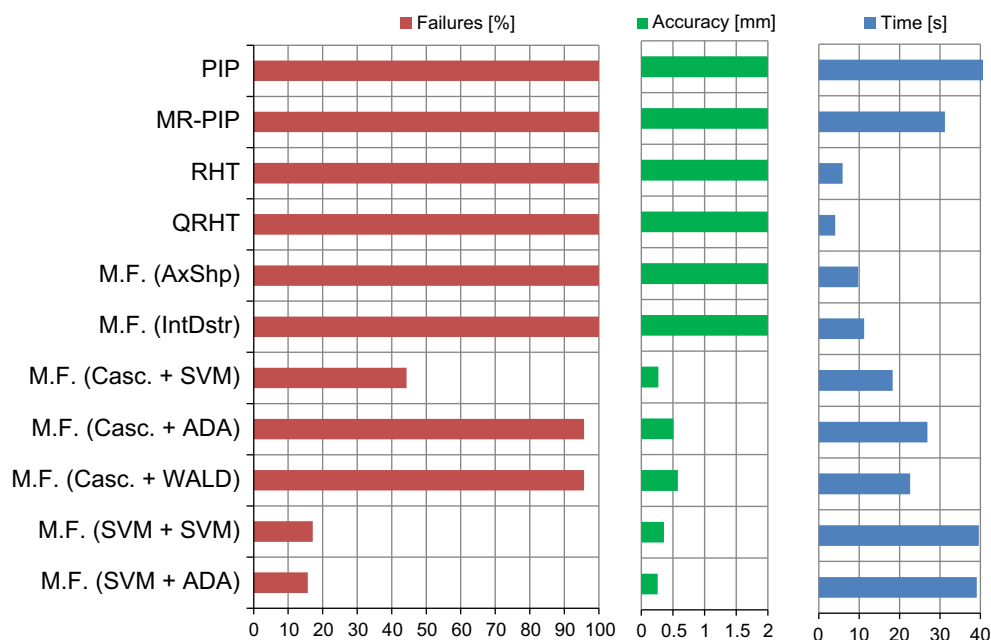


**Fig. 7.** The results of the tool localization on simulated data with low CR ( $CR=1.1$ ). M.F. stands for model-fitting (RANSAC) methods. The first column is the failure rate for all the methods expressed as a percentage; the second column is the axis accuracy in mm; the third column is the calculation time for each method.

insignification angles were acquired using the Voluson 530D ultrasound scanner with 7.5-MHz probe. These volumes have different angle spans of observed volume, listed in pairs  $[\alpha, \beta]$  as  $[20^\circ, 90^\circ]$ ,  $[25^\circ, 80^\circ]$ ,  $[15^\circ, 60^\circ]$ , and  $[25^\circ, 10^\circ]$ ; the definition of  $\alpha$  and  $\beta$  is shown in Fig. 4.

**Breast biopsy:** We tested the method on three real data sets of live breast tissue (Fig. 3) with an 11-gauge straight biopsy needle (1 mm outer diameter). Three-dimensional US images were acquired using the GE Voluson E8 scanner with a 12-MHz probe. The size of all volumes was  $273 \times 383 \times 208$  voxels.

The needle position for real data sets was determined as an average location given by eight observers. The mean variability for human observers was less than 0.4 mm.

## 5.2. Tool localization – testing the complete chain

The complete proposed localization method was evaluated in terms of the axis accuracy, the failure rate, and the elapsed time. Axis accuracy  $\epsilon_{\text{axis}}$  is defined as the maximum Euclidean distance

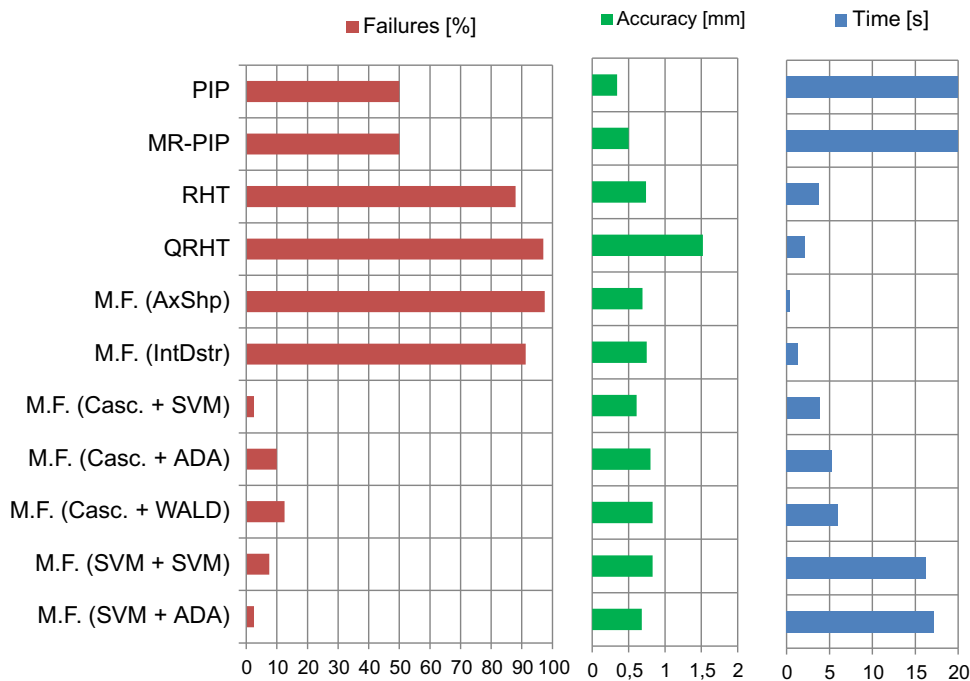
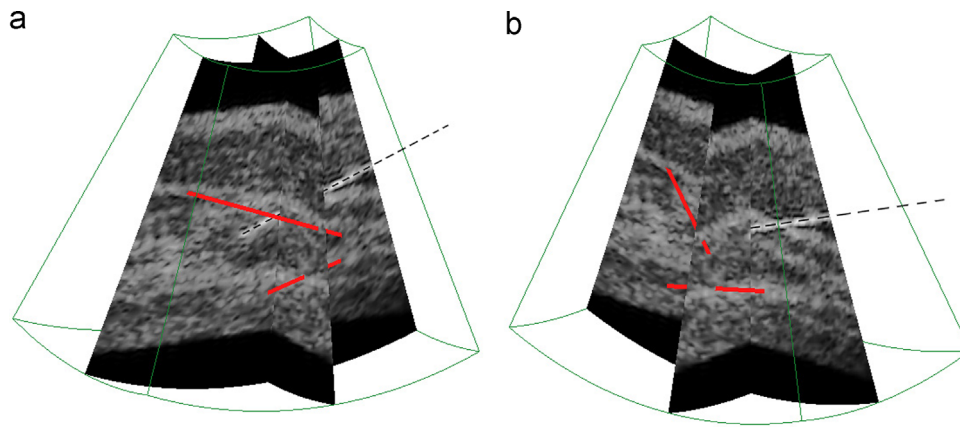


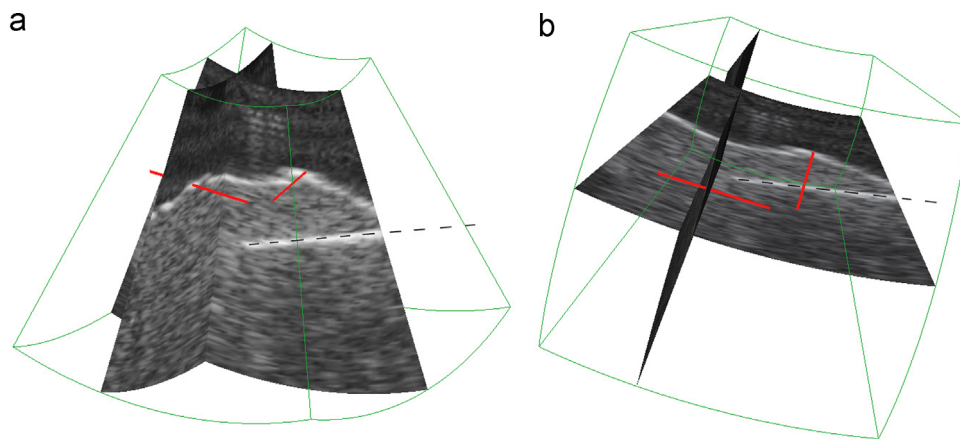
Fig. 8. The results of tool localization on the PVA cryogel phantom. The first column is the failure rate for all the methods expressed as a percentage; the second column is the axis accuracy in mm; the third column is the calculation time for each method.



Fig. 9. The results of tool localization on real data of breast biopsy. The first column is the failure rate for all the methods expressed as a percentage; the second column is the axis accuracy in mm; the third column is the calculation time for each method.



**Fig. 10.** Visualization of the localization results in simulated 3D US data with a low CR. The dashed line shows the correct position computed using model fitting with line filtering (using SVM classifiers). Two red lines show examples of failures without line filtering (tool model AxShp [20]). Two different views (a) and (b) show the same data set in different orientations. (For interpretation of the references to color in this figure caption, the reader is referred to the web version of this article.)



**Fig. 11.** Visualization of the localization results in 3D US data of the PVA phantom. The dashed line shows the correct tool position computed using model fitting with line filtering (using SVM classifiers). Two short red lines show examples of failures without line filtering – the localization method was confused by the high intensity layer on the top. Two different views (a) and (b) show the same data set in different orientations. (For interpretation of the references to color in this figure caption, the reader is referred to the web version of this article.)

of the true tool endpoints from the estimated tool axis:

$$\varepsilon_{axis} = \max\{\|E - Q_1\|, \|T - Q_2\|\} \quad (16)$$

where  $E$  is the true intercept point;  $T$  is the true tool's tip, and  $Q_1$  and  $Q_2$  are the orthogonal projections of  $E$  and  $T$  on the estimated axis  $a(t)$  (see Fig. 5).

In [19], it is claimed that for clinical biopsies, an error of a few millimeters can be acceptable. Consequently, the localization was considered to be a failure when the axis accuracy  $\varepsilon_{axis}$  was greater than a threshold (set at 3 mm) and failures were excluded from accuracy calculations.

We considered two classifiers for the segmentation step: (i) a cascaded classifier denoted CASC and (ii) a linear SVM classifier denoted SVM; and three inlier classifiers for the axis estimation step: (i) a linear SVM classifier denoted SVM, (ii) AdaBoost denoted ADA, and (iii) WaldBoost denoted WALD. These constitute six variants of the proposed method.

The proposed line-filtering method (Section 3.2) was compared to two variants (AxShp and IntDstr) of the previously described RANSAC localization method [20], the parallel integral projection method (PIP) [14] and its multi-resolution variant MR-PIP [17], and the randomized Hough transform (RHT) and its quick variant (Q-RHT) [12]. The times reported include line filtering and pre-processing.

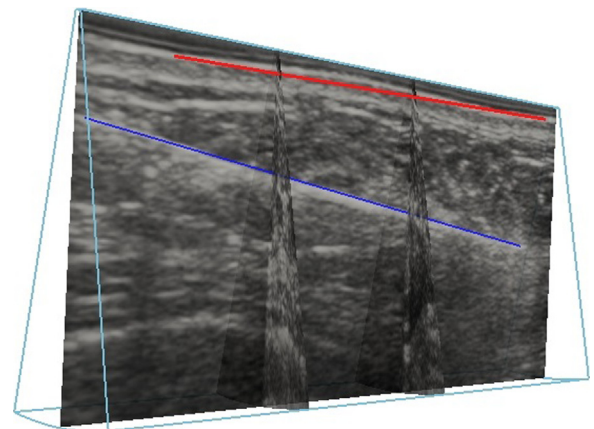


**Fig. 12.** Visualization of the localization results in 3D US data of the breast biopsy. The blue line shows the correct tool position computed using model fitting with line filtering (using SVM classifiers). The red lines show examples of failures without line filtering – the localization method was confused by the high intensity layer on the top. (For interpretation of the references to color in this figure caption, the reader is referred to the web version of this article.)

### 5.3. Tool localization on the simulated data

The CR given by (11) is used to define image quality. The results (axis accuracy, number of failures, time) for high CR data (see



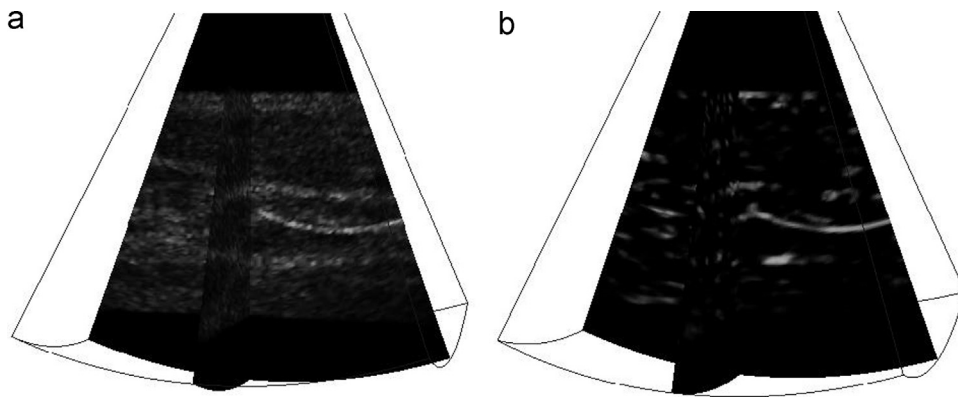


**Fig. 13.** Example of the line-filtering results with a curved needle: (a) original 3D US image simulated using FIELD II and (b) the output of line filtering using Frangi's method.

Fig. 1a for an example) are reported in Fig. 6. The projection (PIP) methods are the slowest and the Hough transform (RHT) methods have the highest number of failures. Previously described RANSAC-based methods [20] are the fastest and have a small number of failures. The new method using line filtering has no failures at all and with the cascade classifier it can be as fast as the earlier methods [20].

Fig. 7 shows the results for more difficult synthetic data with a low CR (see Fig. 10 for an example). The methods not using line filtering fail in all cases. The best performance among line-filtering methods is achieved using the SVM+ADA classifier for both stages; the following is the SVM+SVM classifier. The cascaded classifier decreases the overall time but increases the number of failures.

#### 5.4. Tool localization on real data

The results on real data of the PVA phantom are shown in Fig. 8 and an example of a localization result with and without line filtering is shown in Fig. 11. All methods not using line filtering fail in 50–100% of cases, mostly because of a presence of a highly echogenic 2D interface. The best performance with respect to the number of failures is achieved by combining the Casc+SVM classifier and the SVM+ADA classifiers. The use of a cascade classifier in the pre-segmentation phase reduces the calculation time; consequently, considering the time aspect, the Casc+SVM classifier is better than the SVM+ADA classifier.

Finally, the results on the three breast biopsy data sets are presented in Fig. 9. An example of a localization result using the previous method and an example of the line-filtering localization method are demonstrated in Fig. 12. Methods not using line filtering fail completely. Among the line-filtering methods, combining SVM and AdaBoost classifiers works best. Although the combination of two linear SVM classifiers has a greater than 50% failure rate, the accuracy is slightly better than the SVM+ADA classifier.

## 6. Discussion

The line-filtering method presented herein works with the assumption that the needle is straight. It is also capable of enhancing the contrast between needle and background in the case of C-like deformation or deformation of a higher degree, which is typical for thin micro-electrodes. However, in this paper the method's model-fitting step uses  $n=2$  and only non-curved tools are detected. Extending model fitting to larger  $n=3$  (quadratic curves), using the result of locally line-filtered 3D volume will make it possible to detect curved tools. Table 7 shows the mean contrast ratio improvement using the three line-enhancement

method (see [22, 30, 31]). The best improvement in CR is still obtained with Frangi's measurement. Fig. 13 demonstrates one example with a curved needle in which line filtering improves the contrast of the tool under the assumption of local linearity. Note, however, that in biopsies, the needle is quite thick and bending of the needle is extremely rare.

## 7. Conclusions

We have proposed a new method for tool localization in 3D US volumes that exploits the tool's predominantly 1D shape both when initially selecting tool candidate voxels and when evaluating voxels consistent with particular tool positions. Robustness is significantly improved with respect to our earlier method [20] and to other existing algorithms (Parallel Integral Projection and Randomized Hough Transform).

The best performance in terms of robustness was obtained with SVM classifiers. For data sets with relatively low noise and low clutter, a cascaded classifier approach performs almost as well with greatly reduced computational complexity.

## Conflict of interest statement

None declared.

## Acknowledgments

This study was conducted within the framework of the LabEx CeLyA ("Centre Lyonnais d'Acoustique", ANR-10-LABX-60), LabEx PRIMES (ANR-11-LABX-0063) and the Czech Science Foundation project P202/11/0111. The 3D US breast biopsy and turkey breast data were kindly provided by D. Buckton and C. Perrey from the GE Medical Systems.

## References

- [1] N. Abolhassani, R. Patel, M. Moallem, Needle insertion into soft tissue: a survey, *Medical Engineering and Physics* 29 (4) (2007) 413–431.
- [2] A. Abati, A. Simsir, Breast fine needle aspiration biopsy: prevailing recommendations and contemporary practices, *Clinics in Laboratory Medicine* 25 (4) (2005) 631–654.
- [3] G.S. Merrick, W.M. Butler, K.E. Wallner, R.W. Galbreath, E. Adamovich, Monotherapy brachytherapy for clinically organ-confined prostate cancer, *West Virginia Medical Journal* 101 (4) (2005) 168–171.
- [4] K. Kern, Sentinel lymph node mapping in breast cancer using subareolar injection of blue dye, *Journal of the American College of Surgeons* 189 (6) (1999) 539–545.
- [5] R.L. Alterman, D. Sterio, A. Beric, P.J. Kelly, Microelectrode recording during posteroventral pallidotomy, *Neurosurgery* 44 (2) (1999) 315–321.

- [6] V. Horsley, R.H. Clarke, The structure and functions of the cerebellum examined by a new method, *Brain* 31 (1908) 45–124.
- [7] T.M. Peters, Image-guidance for surgical procedures, *Physics in Medicine and Biology* 51 (14) (2006) R505–R540.
- [8] J.W. Cannon, J.A. Stoll, I.S. Salgo, Real time 3-dimensional ultrasound for guiding surgical tasks, *Computer Aided Surgery* 8 (2003) 82–90.
- [9] S.H. Okazawa, R. Ebrahimi, J. Chuang, R.N. Rohling, S.E. Salcudean, Methods for segmenting curved needles in ultrasound images, *Medical Image Analysis* 10 (3) (2006) 330–342.
- [10] M. Ding, Z. Wei, L. Gardi, D.B. Downey, A. Fenster, Needle and seed segmentation in intra-operative 3D ultrasound-guided prostate brachytherapy, *Ultrasonics* 44 (1) (2006) 331–336.
- [11] M. Aboofazeli, P. Abolmaesumi, P. Mousavi, G. Fichtinger, A new scheme for curved needle segmentation in three-dimensional ultrasound images, in: *Sixth IEEE International Symposium on Biomedical Imaging: From Nano to Macro (ISBI)*, 2009, pp. 1067–1070.
- [12] H. Zhou, W. Qiu, M. Ding, S. Zhang, Automatic needle segmentation in 3D ultrasound images using 3D improved Hough transform, in: *Proceedings of the SPIE Medical Imaging, Parallel Processing of Images, and Optimization Techniques (MIPPR)*.
- [13] H.R.S. Neshat, R.V. Patel, Real-time parametric curved needle segmentation in 3D ultrasound images, in: *Second IEEE RAS & EMBS International Conference on Biomedical Robotics and Biomechatronics*, IEEE press, 2008, pp. 670–675.
- [14] M. Barva, M. Uherčík, J.-M. Mari, J. Kybic, J.-R. Duhamel, H. Liebgott, V. Hlaváč, C. Cachard, Parallel integral projection transform for straight electrode localization in 3-d ultrasound images, *IEEE Transactions on Ultrasonics, Ferroelectrics and Frequency Control* 55 (7) (2008) 1559–1569.
- [15] S. Helgason, *The Radon Transform*, 2nd Edition, Birkhauser Boston, New York, USA, 1999.
- [16] W. Qiu, M. Ding, M. Yuchi, Needle segmentation using 3D quick randomized Hough transform, in: *First International Conference on Intelligent Networks and Intelligent Systems, ICINIS'08*, 2008, pp. 449–452.
- [17] M. Uherčík, J. Kybic, H. Liebgott, C. Cachard, Multi-resolution parallel integral projection for fast localization of a straight electrode in 3D ultrasound images, in: *5th IEEE International Symposium on Biomedical Imaging: From Nano to Macro (ISBI)*, IEEE, 2008, pp. 33–36.
- [18] P.M. Novotny, J.A. Stoll, N.V. Vasilyev, P.J. del Nido, P.E. Dupont, R.D. Howe, GPU based real-time instrument tracking with three dimensional ultrasound, *Medical Image Analysis* 11 (5) (2007) 458–464.
- [19] J.M. Mari, C. Cachard, Ultrasonic scanning of straight micro tools in soft biological tissues: methodology and implementation, *Ultrasonics* 51 (5) (2011) 632–638.
- [20] M. Uherčík, J. Kybic, H. Liebgott, C. Cachard, Model fitting using RANSAC for surgical tool localization in 3-D ultrasound images, *IEEE Transactions on Biomedical Engineering* 57 (8) (2010) 1907–1916.
- [21] M.A. Fischler, R.C. Bolles, Random sample consensus: a paradigm for model fitting with applications to image analysis and automated cartography, *Communications of the ACM* 24 (6) (1981) 381–395.
- [22] A.F. Frangi, W.J. Niessen, K.L. Vincken, M.A. Viergever, Multiscale vessel enhancement filtering, in: *Medical Image Computing and Computer-Assisted Intervention-MICCAI'98*, Springer, 1998, pp. 130–137.
- [23] S. Chaudhuri, S. Chatterjee, N. Katz, M. Nelson, M. Goldbaum, Detection of blood vessels in retinal images using two-dimensional matched filters, *IEEE Transactions on Medical Imaging* 8 (3) (1989) 263–269.
- [24] A.D. Hoover, V. Kouznetsova, M. Goldbaum, Locating blood vessels in retinal images by piecewise threshold probing of a matched filter response, *IEEE Transactions on Medical Imaging* 19 (3) (2000) 203–210.
- [25] W.T. Freeman, E.H. Adelson, The design and use of steerable filters, *IEEE Transactions on Pattern Analysis and Machine Intelligence* 13 (9) (1991) 891–906.
- [26] G. González, F. Aguet, F. Fleuret, M. Unser, P. Fua, Steerable features for statistical 3D dendrite detection, in: *Proceedings of MICCAI*, Springer-Verlag, 2009, pp. 625–632.
- [27] S. Aylward, E. Bullitt, S. Pizer, D. Eberly, Intensity ridge and widths for tubular object segmentation and description, in: *Proceedings of the Workshop on Mathematical Methods in Biomedical Image Analysis*, IEEE, 1996, pp. 131–138.
- [28] J. Staal, M.D. Abràmoff, M. Niemeijer, M.A. Viergever, B. van Ginneken, Ridge-based vessel segmentation in color images of the retina, *IEEE Transactions on Medical Imaging* 23 (4) (2004) 501–509.
- [29] M. Uherčík, *Surgical Tools Localization in 3D Ultrasound Images*, Research Report, INSA de Lyon, Prague, Czech Republic, April 2011.
- [30] Q. Li, S. Sone, K. Doi, Selective enhancement filters for nodules, vessels, and airway walls in two- and three-dimensional CT scans, *Medical Physics* 30 (8) (2003) 2040–2051.
- [31] Y. Sato, S. Nakajima, N. Shiraga, H. Atsumi, S. Yoshida, T. Koller, G. Gerig, R. Kikinis, Three-dimensional multi-scale line filter for segmentation and visualization of curvilinear structures in medical images, *Medical Image Analysis* 2 (2) (1998) 143–168.
- [32] M. Barva, *Localization of Surgical Instruments in 3D Ultrasound Images*, Ph.D. Thesis CTU-CMP-2007-12, Center for Machine Perception, K13133 FEE Czech Technical University, Prague, Czech Republic, June 2007.
- [33] R.O. Duda, P.E. Hart, D.G. Stork, *Pattern Classification*, 2nd Edition, Wiley-Interscience, 2000.
- [34] S.I. Gallant, Perceptron-based learning algorithms, *IEEE Transactions on Neural Networks* 1 (2) (1990) 179–191.
- [35] V. Franc, S. Sonnenburg, OCAS optimized cutting plane algorithm for support vector machines, in: *Proceedings of ICML*, 2008, pp. 320–327.
- [36] Y. Freund, R.E. Schapire, A decision-theoretic generalization of on-line learning and an application to boosting, *Journal of Computer and System Sciences* 55 (1997) 119–139.
- [37] T. Svoboda, J. Kybic, V. Hlaváč, *Image Processing, Analysis & Machine Vision-A MATLAB Companion*, 1st Edition, Thomson, Toronto, Canada, 2007.
- [38] J. Sochman, J. Matas, Waldboost-learning for time constrained sequential detection, in: *IEEE Computer Society Conference on Computer Vision and Pattern Recognition, CVPR 2005*, vol. 2, IEEE Computer Society, Washington, DC, USA, 2005, pp. 150–156.
- [39] R.E. Schapire, Y. Singer, Improved boosting algorithms using confidence-rated predictions, *Machine Learning* 37 (1999) 297–336.
- [40] J.A. Nelder, R. Mead, A simplex method for function minimization, *The Computer Journal* 7 (1965) 308–313.
- [41] J.A. Jensen, Field: a program for simulating ultrasound systems, in: *Tenth Nordicbaltic Conference On Biomedical Imaging*, vol. 34, Springer, New York, 1996, pp. 351–353.
- [42] J.A. Jensen, N.B. Svendsen, Calculation of pressure fields from arbitrarily shaped, apodized, and excited ultrasound transducers, *IEEE Transactions on Ultrasonics, Ferroelectrics and Frequency Control* 39 (2) (1992) 262–267.
- [43] F. Duboeuf, A. Basarab, H. Liebgott, E. Brusseau, P. Delachartre, D. Vray, Investigation of PVA cryogel Young's modulus stability with time, controlled by a simple reliable technique, *Medical Physics* 36 (2) (2009) 656–661.